International Journal of Nanomedicine

Dovepress

open access to scientific and medical research

Open Access Full Text Article

ORIGINAL RESEARCH

Flexible Hollow Human Serum Albumin-Catalase Nanocapsules with High Accumulation and Uptake Ability for Enhanced Photodynamic Therapy

Yuyuan Shi[1,*], Ying Zhao[2,*], Wen Kang[2], Wei Lu[3], Dong Chen[3], Jun Tao[3], Jing Li[3], Ruifa Yu[3], Jiajia Zhao[3], Rui Tang[3], Zhaogang Teng[3], Lixing Weng[1]

[1]College of Geography and Biological Information, Nanjing University of Posts and Telecommunications, Nanjing, People's Republic of China; [2]Department of Radiology, Nanjing First Hospital, Nanjing Medical University, Nanjing, People's Republic of China; [3]Key Laboratory for Organic Electronics & Information Displays and Jiangsu Key Laboratory for Biosensors, Institute of Advanced Materials, Jiangsu National Synergetic Innovation Centre for Advanced Materials, Nanjing University of Posts and Telecommunications, Nanjing, People's Republic of China

*These authors contributed equally to this work

Correspondence: Zhaogang Teng; Lixing Weng, Email iamzgteng@njupt.edu.cn; lxweng@njupt.edu.cn

Introduction: Photodynamic therapy (PDT) has attracted increasing attention for tumor treatment because of its minimal invasiveness and specific spatiotemporal selectivity. However, insufficient tumor accumulation and low cellular uptake of photosensitizers limit its therapeutic efficacy.

Methods: In this study, flexible hollow human serum albumin/catalase nanocapsules (HSA/CATs) were created using a core-assisted protein-coating method and combined with the photosensitizer chlorin e6 (HSA/CAT@Ce6) for PDT.

Results and Discussion: Transmission electron microscopy (TEM) images demonstrate that HSA/CAT nanocapsules are flexible, with a uniform diameter (310 nm) and a well-defined hollow structure. Thanks to their flexibility, HSA/CAT@Ce6 nanocapsules show a higher cellular uptake than rigid nanoparticles. The nanocapsules effectively generate reactive oxygen species (ROS) in 4T1 cells because of their high cellular uptake and catalytic capacity, remarkably enhancing their in vitro PDT efficacy. In addition, the in vivo tumor accumulation of HSA/CAT@Ce6 nanocapsules is significantly larger than that of rigid nanoparticles and Ce6, meaning they are highly effective in tumor cell ablation. This demonstrates that our flexible nanoplatform holds great promise for enhancing PDT of tumor.

Keywords: flexible nanoplatform, human serum albumin, sufficient tumor accumulation, high cellular uptake, photodynamic therapy

Introduction

According to the statistics of the International Agency for Research, malignant tumors are having an increasingly wide impact on human health.[1] Traditionally, chemotherapy, radiotherapy, and surgery are used in tumor therapy. However, these therapeutic strategies are limited by their own insurmountable shortcomings, such as systemic side effects and high recurrence rates.[2] Recently, photodynamic therapy (PDT), a noninvasive method, has attracted increasing attention in the context of tumor treatment.[3,4] In essence, PDT ablates tumors through the use of cytotoxic reactive oxygen species (ROS) produced from photosensitizers (PSs) exposed to laser irradiation. Compared with traditional treatment, PDT has the advantages of low invasiveness, good repeatability, and little cumulative toxicity. It has been proved effective in the treatment of many kinds of cancer over the last few decades, such as superficial bladder cancer, Barrett's esophageal cancer, and skin cancer.[2] However, many studies have shown that the low tumor accumulation and cellular uptake of photosensitizers greatly reduces PDT efficacy.[5–9] In addition, the efficiency of PDT is also seriously limited by the hypoxic microenvironment of solid tumors.[3,10,11] Therefore, there is an urgent need to resolve these obstacles in PDT.

Therapeutic nanoplatforms have attracted extensive interest in tumor therapy because of their excellent tumor targeting, efficient drug delivery, and comprehensive functions. Such nanoplatforms, with various properties and functions, have been

Received: 14 October 2022
Accepted: 19 January 2023
Published: 29 January 2023

explored and used in tumor treatment fields.[12–14] Among them, flexible nanoplatforms have attracted increasing attention because they have a larger drug loading space, longer blood persistence, and higher cellular uptake efficiency than solid nanoplatforms. For example, Teng et al found that deformable hollow periodic mesoporous organosilica were easily engulfed by MCF-7 cells via a spherical-to-oval morphology change, which increased cellular uptake by up to 26 fold.[15] Yu et al demonstrated that semi-elastic nanoparticles surmounted multiple intestinal barriers more efficiently than rigid nanoparticles, effectively increasing the bioavailability of doxorubicin.[16] Inspired by these works, we believe that significant potential exists in using flexible hollow nanoplatforms to enhance PDT efficacy. However, to the best of our knowledge, flexible nanoplatforms have not been prepared for tumor PDT.[15,17–21]

In recent years, protein materials have been widely used in preparing therapeutic nanoplatforms because of their excellent biocompatibility and enzymic activity.[22–25] For example, human serum albumin (HSA), as a natural drug carrier with a high in vivo stability and excellent tumor targeting ability, has been used in clinical settings.[26,27] In addition, several proteins with enzymic activity have played an important role in tumor treatment. For instance, catalase (CAT) has been used to overcome the hypoxic microenvironment in PDT by converting endogenous hydrogen peroxide into water and oxygen.[28–30] Considering the advantages, there is considerable research potential in constructing a flexible platform using HSA and CAT to improve the tumor targeting and cellular uptake of photosensitizers, and to convert endogenous hydrogen peroxide to oxygen, thus improving PDT efficacy.

We successfully prepared a flexible hollow human serum albumin/catalase nanoplatform (HSA/CAT) using a core-assisted protein-coating approach, and then loaded photosensitizer Ce6 (HSA/CAT@Ce6) for PDT. The flexible HSA/CAT nanocapsules are uniform in size (about 310 nm), have a well-defined hollow structure, and are flexible. As-prepared HSA/CAT@Ce6 nanocapsules exhibit higher cellular uptake than their solid counterparts for tumor cells because of the targeting function and flexibility of HSA. Moreover, HSA/CAT@Ce6 can effectively convert tumoral endogenous hydrogen peroxide to oxygen, increasing ROS after exposure to laser irradiation. Furthermore, HSA/CAT@Ce6 has a high tumor accumulation in a tumor-bearing mouse model after its intravenous injection, exhibiting excellent in vivo PDT efficacy after laser irradiation.

Materials and Methods

Materials

Cetyltrimethylammonium bromide (CTAB), tetraethoxysilane (TEOS), anhydrous ethanol, a concentrated ammonia aqueous solution (25 wt%), glutaraldehyde (GA, 25%), and hydrofluoric acid (HF, 48 wt% in H_2O) were purchased from Sinopharm Chemical Reagent Co., Ltd. (Shanghai, China). N, N-dimethylformamide (DMF), phosphate buffer saline (PBS), N-hydroxysulfosuccinimide (NHS), N-(3-dimethylaminopropyl)-N′-ethylcarbodiimide hydrochloride (EDC), catalase (CAT), chlorin e6 (Ce6), hydrogen peroxide (H_2O_2), 2',7'-dichlorofluorescin diacetate (DCFH-DA), poly (ethylene imine) (PEI, branched, Mw: 25000), and human serum albumin (HSA) were obtained from Sigma-Aldrich (St. Louis, MO, USA). Singlet oxygen sensor green (SOSG) was purchased from Invitrogen (USA). 4'-6-diamidino-2-phenylindole (DAPI) were purchased from Nanjing Keygen Biotech. Co., Ltd. (Nanjing, China). Roswell Park Memorial Institute (RPMI) 1640 medium, cell counting kit-8 (CCK-8), and fetal bovine serum (FBS) were purchased from Gibco Laboratories (NY, USA). The water used in all experiments is deionized water with a resistivity of 18 MΩ cm.

Preparation of Mesoporous Silica Nanoparticles (MSNs)

Mesoporous silica nanoparticles (MSNs) are prepared by a surfactant-directed sol-gel procedure using cetyltrimethylammonium bromide (CTAB) as a template and tetraethoxysilane (TEOS) as a silica source.[22,31] Firstly, 0.16 g of CTAB was dissolved in a mixed solution of 30 mL of ethanol, 75 mL of water, and 0.5 mL of concentrated aqueous ammonia. The mixture was then put into a 35°C water bath, to which 0.5 mL TEOS were added. After stirring at 500 rpm for 3 h, the white suspension was centrifuged at 10,000 rpm for 10 min, washed three times with ethanol, and finally dispersed in 10 mL of ethanol. In order to remove the CTAB surfactant, the products were dispersed in 200 mL of ethanol solution with 400 μL of concentrated hydrochloric acid and stirred in a 60°C water bath. To completely remove any traces of the

CTAB surfactant, the extraction procedure was repeated three times. After washing them twice with ethanol and then twice with water, the MSNs without CTAB were dispersed in 12.5 mL of deionized water to obtain an MSN solution.

Preparation of HSA/CAT

Firstly, 4 mL of the prepared MSN aqueous solution was mixed with 20 mL of 1 mg/mL aqueous PEI solution. After standing for 20 min and then washing with water three times, PEI-modified MSNs (MSNs-PEI) were obtained. Afterwards, 10 mL of aqueous MSNs-PEI were mixed with 10 mL of aqueous GA. After shaking at room temperature for 12 h (200 times/min), the products were washed with water three times and aqueous MSNs-PEI-GA was obtained. Ten mL of aqueous HSA (4 mg/mL) and 10 mL of aqueous CAT (1 mg/mL) were then added to the aqueous MSNs-PEI-GA. After shaking for 12h at a speed of 200 times/min, the products were centrifuged, washed with water, and dispersed in 10 mL of water to form aqueous MSNs-HSA/CAT. HF (40 wt%) was added to the MSNs-HSA/CAT aqueous solution and pipetted for 1 min to remove the MSN templates. Finally, the HSA/CAT nanocapsules were washed with water three times and dispersed in 10 mL of water. Similarly, if aqueous CAT is not added to aqueous HSA (4 mg/mL), hollow HSA nanocapsules can be obtained.

Preparation of HSA/CAT@Ce6, MSNs-HSA/CAT@Ce6 and HSA@Ce6

The preparation procedure for HSA/CAT@Ce6 is as follows: Ten mg of Ce6, 5 mg of EDC, and 5 mg of NHS were dissolved in 1.5 mL of DMF. The mixture was shaken in the dark for 3 h. Afterwards, 10 mL of HSA/CAT aqueous solution was added to the mixture, which was then shaken for a further 12 h in the dark. Finally, the HSA/CAT@Ce6 products were collected by centrifugation, washed successively with DMF and PBS, and dispersed in 7 mL of PBS. MSN-HSA/CAT@Ce6 could be obtained by the same method by changing HSA/CAT aqueous solution to aqueous MSNs-HSA/CAT. HSA@Ce6 is obtained through the same synthesis method by changing HSA/CAT aqueous solution to hollow HSA nanocapsules.

Characterization

TEM images were captured using an HT7700 microscope (Hitachi, Tokyo, Japan) at 100 kV. The zeta potential and hydrodynamic sizes were measured using a Brookhaven ZetaPALS (Brookhaven Instruments Co., Holtsville, NY, USA). UV-vis spectra were obtained using a Lambda 35 UV-vis spectrophotometer (PerkinElmer, Inc., Waltham, MA, USA). FT-IR spectra were recorded on a Nicolet Nexus 870 spectrometer (Nicolet Instruments Inc., Madison, WI, USA).

Evaluation of Catalase Activity

To demonstrate that flexible HSA/CAT@Ce6 could catalyze hydrogen peroxide to produce oxygen, oxygen bubbles were detected by co-incubating CAT, Ce6, and the nanocapsules with hydrogen peroxide, respectively. CAT (1 mg/mL, 5 mL), Ce6 (30 μg/mL, 5 mL), and HSA/CAT@Ce6 (Ce6 equivalent to 30 μg/mL, 5 mL) were incubated with hydrogen peroxide (3.0 wt%) at 37°C for 30 min. CAT (1 mg/mL, 5 mL), Ce6 (30 μg/mL, 5 mL), and HSA/CAT@Ce6 (Ce6 equivalent to 30 μg/mL, 5 mL) were incubated without hydrogen peroxide as control. Then, the tubes were photographed to observe the occurrence of bubbles.

Commercial oxygen probe $[(Ru(dpp)_3)]Cl_2$ was used to detect the catalase-like capacity of HSA/CAT@Ce6. The fluorescence intensity of the probe decreased with the generation of O_2. Fifty μL each of Ce6, MSN-HSA/CAT@Ce6, HSA@Ce6, and HSA-CAT@Ce6 were mixed with 50 μL H_2O_2 (3.0 wt%) (Ce6 equivalent to 2 μg/mL), and to this mixture, 10 μL of $[(Ru(dpp)_3)]Cl_2$ (10 μg/mL) was added. After the mixed solution was incubated at 37°C for 30 min, the fluorescence intensity of each well at Ex/Em = 455/613 nm was measured using a multifunctional microplate reader (Tecan Infinite PRO TWIN 200, Switzerland). Each group was set up six complex wells.

Determination of ROS Generation

In order to detect the ROS generated by the HSA/CAT@Ce6 and their evolution over time, 100 μL of HSA/CAT@Ce6 (Ce6 equivalent to 3 μg/mL) and 50 μL of SOSG (50 μM) were mixed in a 96-well plate with or without hydrogen peroxide (3 wt%). Each well was irradiated with a 660 nm laser at a power of 0.5 W/cm^2 for 0, 1, 3, 5, and 10 min. The fluorescence emission intensity of the mixture was recorded at a wavelength of 530 nm using a multifunctional microplate reader (Tecan Infinite PRO TWIN 200, Switzerland), and the excitation wavelength was set to 490 nm.

To detect the ROS produced by HSA/CAT@Ce6 for different hydrogen peroxide concentrations, 100 μL of HSA/CAT@Ce6 (Ce6 equivalent to 3 μg/mL) and 50 μL of SOSG (50 μM) were mixed and 1.5 wt%, 3 wt% and 6 wt% of H_2O_2, respectively. Each well was irradiated with a 660 nm laser at a power of 0.5 W/cm^2 for 3 min. The fluorescence emission intensity of the mixture was recorded at a wavelength of 530 nm using an excitation wavelength of 490 nm.

The ROS generated within the cells were detected using 2',7'-dichlorofluorescein diacetate (DCFH-DA). 4T1 cells (Procell Life Science &Technology, Wuhan, China) were seeded in 96 well plates with a density of 2×10^4 cells per well for 24 h, and then incubated with PBS, Ce6, MSN-HSA/CAT@Ce6, HSA@Ce6 and HSA-CAT@Ce6 (Ce6 equivalent to 1.5 μg/mL) for 24 h. Next, the medium was removed, and each well was washed with PBS twice. Roswell Park Memorial Institute (RPMI) 1640 medium (100 μL) containing 20 μM of DCFH-DA was added to the cells and then incubated for 20 min in the dark. After washing it with serum-free RPMI 1640 medium three times, each well was irradiated by a 660 nm laser for 5 min (1 W/cm^2). The generation of intracellular ROS was measured using a microplate reader (Tecan Infinite PRO TWIN 200, Switzerland) to detect the fluorescence intensity (Ex/Em 504 nm/529 nm) of each well.

Cell Viability Assessments

4T1 cells were seeded in a 96-well plate with a density of 2×10^4 cells per well for 24 h. Fresh RPMI 1640 medium (100 μL) with 10% FBS containing various concentrations (0, 12.5, 25, 50, 100, and 200 g/mL) of HSA/CAT or HSA/CAT@Ce6 were added to each well, respectively, and incubated for 24 h. Subsequently, 10 μL of CCK8 was added to each well and the mixture incubated for a further 2 h. The absorbance of the cells per well at 450 nm was recorded using a multifunctional microplate reader (Tecan Infinite PRO TWIN 200, Switzerland). The cell viability was calculated by referring to previous literature.[22]

In vitro Photodynamic Therapy

The 96-well plates containing 4T1 cells were planted for 24 hours at a density of 2×10^4 cells per well. One-hundred mL of fresh medium with 10% FBS containing HSA/CAT@Ce6 at various concentrations (0, 0.2, 0.4, 0.8, 1.6, and 4 μg/mL) were added to the cells and incubated for 24 h. After washing it twice with serum-free RPMI 1640 medium, each well was irradiated by a 660 nm laser for 5 min (1 W/cm^2). Subsequently, the cell viability was evaluated by performing CCK-8 assays.

To explore the role of different components in HSA/CAT@Ce6 for photodynamic therapy, 4T1 cells were seeded in a 96-well plate with a density of 2×10^4 cells per well for 24 h. RPMI 1640 Medium with 10% FBS containing 100 μL of various nanomaterials (Ce6, MSNs-HSA/CAT@Ce6, HSA@Ce6, HSA/CAT@Ce6+HSA, and HSA/CAT@Ce6) with concentration of 1.5μg/mL were added to 96-well plate, and incubated for 24 h. After washing it twice with RPMI 1640 medium, each well was irradiated by a 660 nm laser for 5 min (1 W/cm^2). Then, CCK-8 assays were used to determine the cell viability. Similarly, we irradiated (5 min,1 W/cm^2) the 4T1 cells incubated with different materials at different concentrations (0, 0.1, 0.2, 0.4, 0.8,1.6, 3.2 μg/mL Ce6 equiv.) for 24 hours, and then calculated the cell viability. IC50 of HSA/CAT@Ce6, HSA@Ce6, MSNs-HSA/CAT@Ce6, and Ce6 was calculated using Quest Graph™ IC50 Calculator tool. The PDT effects of HSA/CAT@Ce6 in vitro were studied using normal mammary epithelial cells MCF 10A (Procell Life Science &Technology, Wuhan, China) in a similar way. MCF 10A cells were incubated with HSA/CAT@Ce6 at different concentrations (0, 0.2, 0.4, 0.8,1.6, 3.2 μg/mL Ce6 equiv.) for 24 hours. Each well was washed twice with PBS, and then irradiated for 5 minutes (660nm, 1 W/cm^2). At last, the cell viability was detected by CCK-8 assays.

LIVE/DEAD Cell Imaging Kit (488/570) (Invitrogen) was used to observe the live/dead staining of 4T1 cells. 4T1 cells were seeded in confocal dishes with a density of 2×10^4 cells per dish. After 12 h, the original culture media were replaced with 1 mL of RPMI 1640 medium with 10% FBS containing HSA@Ce6, MSNs-HSA/CAT@Ce6, and HSA/CAT@Ce6 (Ce6 equivalent to 3 μg/mL), respectively. After 12 h of incubation, the cells were washed twice with PBS, and each well was irradiated by a 660 nm laser for 5 min (1 W/cm^2). HSA/CAT@Ce6 without laser irradiation was used as a control. The distribution of living cells and dead cells was observed with fluorescence microscope (Nikon, Japan).

Cellular Uptake

Confocal laser scanning microscope (CLSM) was used to analyze the uptake of Ce6, MSNs-HSA/CAT@Ce6, and HSA/CAT@Ce6 in 4T1 cells. 4T1 cells were seeded in confocal dishes with a density of 2×10^4 cells per dish. After 12 h, the original culture media were replaced with 1 mL of RPMI 1640 medium with 10% FBS containing Ce6, MSNs-HSA/CAT@Ce6, or HSA/CAT@Ce6 (Ce6 equivalent to 3 μg/mL), respectively. After 6 h of incubation, the cells were washed twice with PBS and stained with 2-(4-Amidinophenyl)-6-indolecarbamidine dihydrochloride (DAPI dihydrochloride) for 20 min. The images were obtained using a Nikon A1 CLSM (Nikon, Tokyo, Japan). Correlation analyses were performed using ImageJ Software (ImageJ 1.53t, USA).

The Tumor Model

Female Balb/c mice (5–7 weeks, about 16 g) were provided by the Experimental Animal Center of Nanjing First Hospital of Nanjing Medical University. All animal procedures were performed according to guidelines for Laboratory Animal Welfare in Nanjing Medical University (http://iacuc.njmu.edu.cn:8080/article/list-10018.html) and were approved by the Animal Ethics Committee of Nanjing First Hospital (DWSY-2101557). 4T1 cells (2×10^6 suspended in 100 μL of PBS solution) were subcutaneously injected at the root of the right thigh of each female Balb/c mouse to construct 4T1 tumor-bearing mice. When the tumor grew to about 200 mm^3, the mice were used in the in vivo experiment.

In vivo Biodistribution and Tumor Accumulation

Three 4T1 tumor-bearing mice (tumor volume about 200 mm^3) were injected with Ce6, MSNs-HSA/CAT@Ce6, and HSA/CAT@Ce6 (100 μL, 30 μg/mL Ce6 equiv), respectively. Twenty-four hours after tail vein injection, the mice were euthanized, and the tumors and major organs were excised for optical imaging by an IVIS® spectrum in vivo imaging system (PerkinElmer, America). This was done to record the in vivo biodistribution and tumor accumulation of the nanoplatforms.

In vivo Photodynamic Therapy

Mice bearing 4T1 tumors were randomly divided into five groups (three mice per group) and subjected to the following treatments: (1) PBS, (2) Ce6, (3) MSNs-HSA/CAT@Ce6, (4) HSA@Ce6, and (5) HSA-CAT@Ce6. Therapeutic agents (Ce6 equiv 30 μg/mL, 100 μL) or PBS solution (100 μL) were injected by tail intravenously. After 24 h, the mice were irradiated by a 660 nm laser (1 W/cm^2) for 5 min. Tumor volume and body weight were measured and recorded every other day for 14 days. Tumor volume was calculated according to the following formula: Tumor volume V (mm^3) = $d^2 \times D/2$ (d is the shortest diameter of the tumor and D is the longest diameter).

Histological Analysis

After 14 days' treatment, all mice were euthanized, and the tumors and major organs were excised, dissected, and fixed in 4% formaldehyde for 24 h. After paraffin embedding and H&E staining, the pathological sections of these collected tissues were observed using an inverted microscope (Nikon, Japan).

Results and Discussion

HSA/CAT@Ce6 nanocapsules were synthesized via a core-assisted protein-coating approach (Scheme 1). Monodispersed mesoporous silica nanospheres (MSNs) as a hard core were prepared using a modified surfactant-directed sol-gel procedure with cetyltrimethylammonium bromide (CTAB) as a template and tetraethoxysilane (TEOS) as a silica source.[32–34] PEI was then adsorbed on the surface of the MSNs by electrostatic interaction and modified with GA via a condensation reaction between the aldehyde and amino groups. Next, HSA and CAT proteins were connected with GA to form core-shell structured nanospheres (denoted as MSNs-HSA/CAT). Finally, the MSN spheres inside the MSNs-HSA/CAT were etched away using hydrofluoric acid (HF) to obtain flexible hollow HSA/CAT capsules. To construct a PDT nanoplatform, the photosensitizer chlorin e6 (Ce6) was combined with the HSA/CAT nanocapsules through an amide reaction to form HSA/CAT@Ce6 nanocapsules. When HSA/CAT@Ce6 was intravenously injected into the mice

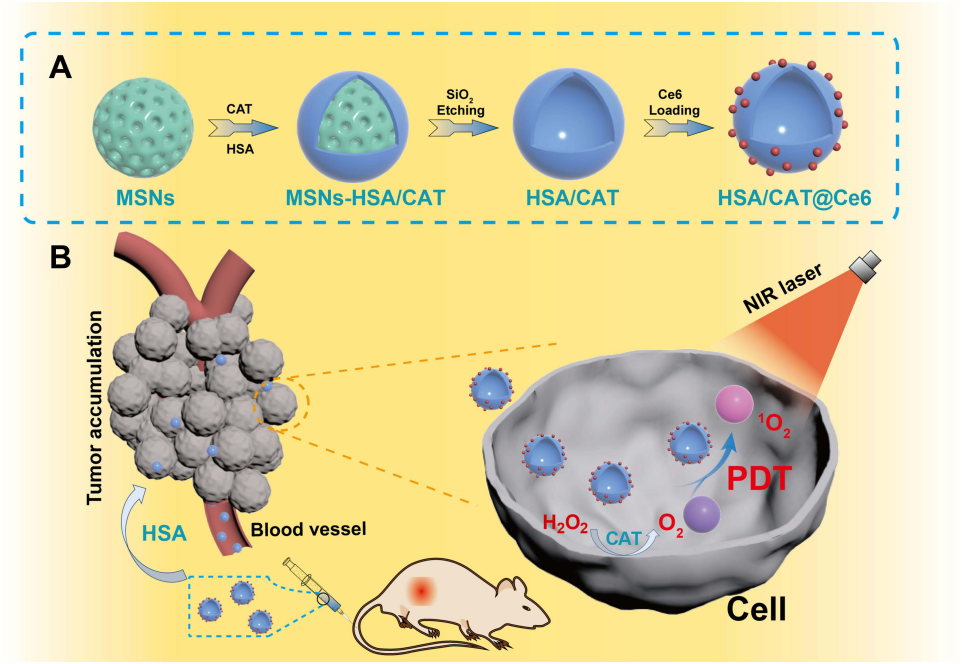

Scheme 1 (**A**) Schematic illustration for the synthesis of flexible hollow HSA/CAT@Ce6 nanocapsules using the core-assisted protein-coating approach. (**B**) Enhanced PDT using the flexible nanoplatforms.

with 4T1 tumors, the targeting ability and flexible structure of the HSA were conducive to a high tumor accumulation and cellular uptake, concentrating the photosensitizer in the tumors. HSA/CAT@Ce6 can convert tumor endogenous hydrogen peroxide to oxygen, which produces more ROS under near-infrared (NIR) exposure, so as to kill tumor cells more effectively.

Transmission electron microscopy (TEM) images show that the MSNs have spherical morphology, uniform size, and good dispersion (Figures 1A and B). After coating HSA and CAT, TEM images show that the uniformity in spherical morphology of the MSNs-HSA/CAT decreased due to the MSN cores being corroded by the acidic GA (Figure 1C and D). After etching by HF, TEM images show that the HSA/CAT protein capsule is hollow inside and wrinkled on the surface, indicating its flexibility and deformability (Figures 1E and F). The average diameter of HSA/CAT is 314 ± 25 nm, while that of MSNs is 262 ± 22 nm. The formation of uniform HSA/CAT hollow nanocapsules rests on the cross-linking of proteins with PEI, ensuring a stable structure after removal of the MSN core. TEM images show that the flexible hollow HSA/CAT nanocapsules remained intact after 28 days of storage in PBS, evidencing their considerable stability (Figure S1). Element mapping images of HSA/CAT show that C and O are evenly distributed on the shell, N elements are distributed in the central area of the shell, and that the Si elements have disappeared, evidence for the formation of hollow protein nanocapsules (Figures 1G and H).

The hydrodynamic diameters of the MSNs, HSA/CAT, and HSA/CAT@Ce6 nanocapsules measured by dynamic light scattering (DLS) are approximately 280, 310, and 330 nm, respectively, indicating that they have excellent dispersion in aqueous solution (Figure 2A). As shown in Figure S2A, the hydrodynamic diameters of MSNs, HSA@Ce6, and HSA/CAT@Ce6 nanocapsules in RPMI 1640 media are approximately 335, 343, and 364 nm, respectively. Figure S2B shows that the hydrodynamic diameters of MSNs, HSA@Ce6, and HSA/CAT@Ce6 nanocapsules in FBS are approximately 365, 420, and 413 nm, respectively. The zeta potential of MSNs, MSNs-PEI, MSNs-PEI-GA, MSNs-HSA/CAT, HSA/CAT, and HSA/CAT@Ce6 were measured to be −28.00 ± 0.71, 58.23 ± 2.21, 43.17 ± 3.09, −14.26 ± 0.26, −22.64 ± 1.13, and −32.82 ± 2.24 mV, respectively, proving the successful modification of PEI, GA, and the HSA/CAT protein layer (Figure 2B). Fourier transform infrared (FT-IR) spectra show that MSNs have an absorption peak corresponding to the Si-O-Si bond at 1050 cm^{-1}, while this peak is absent for HSA/CAT. This absence indicates that the internal mesoporous silica framework has been effectively etched away by the HF, forming the hollow protein structure (Figure 2C). UV-vis spectra show that HSA/CAT@Ce6 has absorption

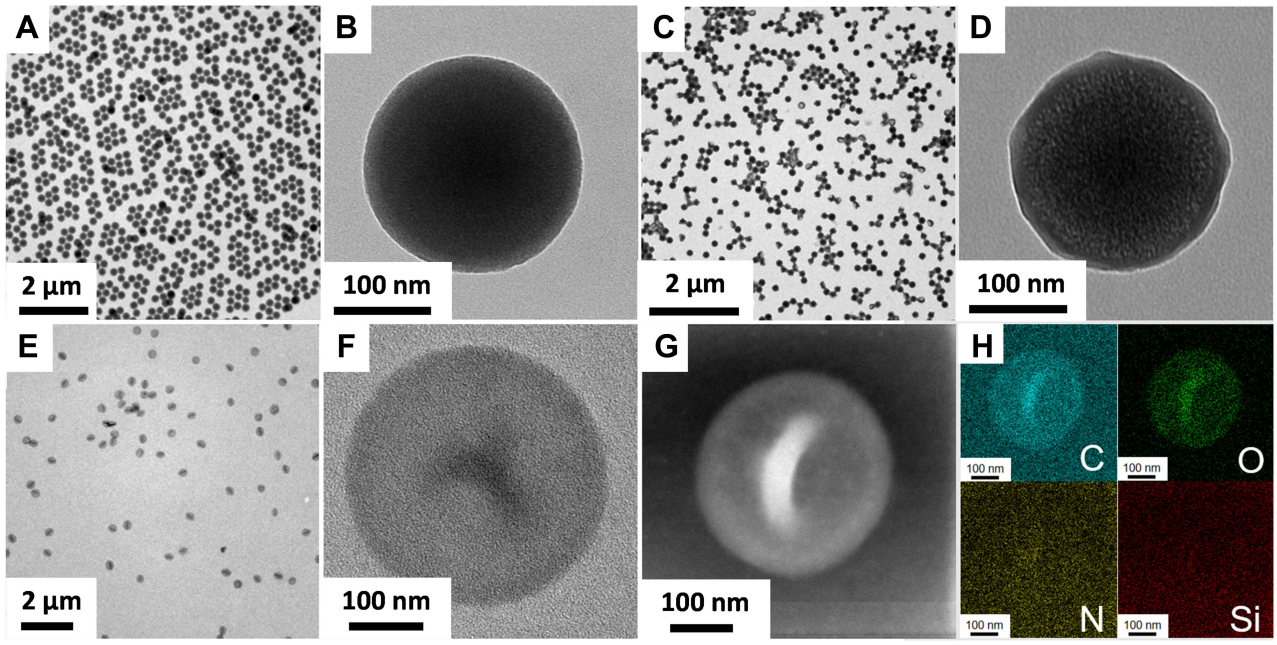

Figure 1 TEM images of the MSNs (**A** and **B**), MSNs-HSA/CAT (**C** and **D**), and HSA/CAT nanocapsules (**E** and **F**). TEM bright-field images (**G**) and corresponding elemental mapping images (**H**) of the flexible hollow HSA/CAT nanocapsules. Blue, green, yellow, and red indicate elements C, O, N, and Si, respectively.

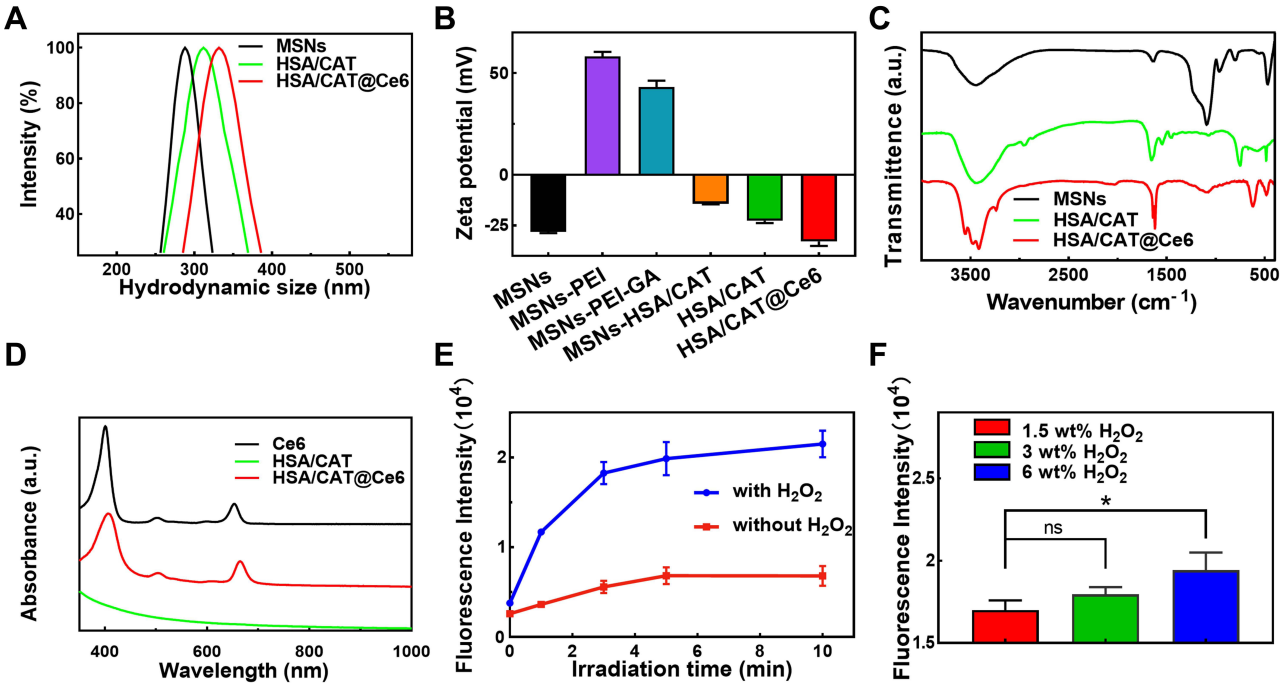

Figure 2 (**A**) DLS of the MSNs, HSA/CAT, and HSA/CAT@Ce6 nanocapsules. (**B**) Zeta potentials of the MSNs, MSNs-PEI, MSNs-PEI-GA, MSNs-HSA/CAT, HSA/CAT, and HSA/CAT@Ce6 in water. (**C**) FT-IR spectra of the MSNs, HSA/CAT, and HSA/CAT@Ce6 nanocapsules. (**D**) UV-vis spectra of the Ce6, HSA/CAT, and HSA/CAT@Ce6. (**E**) Fluorescence intensity of SOSG with laser irradiation (660 nm, 3 min, 1 W/cm^2) after HSA/CAT@Ce6 mixing with or without H_2O_2. (**F**) Fluorescence intensity of SOSG with laser irradiation (660 nm, 3 min, 1 W/cm^2) after HSA/CAT@Ce6 mixing with different concentrations of H_2O_2. *P* values: ns $P > 0.05$, $^*P < 0.05$ are calculated by SPSS with a *t*-test.

peaks corresponding to Ce6 near 660 nm and 400 nm, while HSA/CAT has no absorption signal, indicating that Ce6 is successfully loaded into the HSA/CAT@Ce6 nanocapsules (Figure 2D). It is calculated that drug loading (DL) of Ce6 in HSA/CAT@Ce6 was 2.921% and encapsulation efficiency (EE) of Ce6 in HSA/CAT@Ce6 was 46.74%. ROS, including singlet

oxygen species, play a key role in killing tumor cells in PDT. The CAT contained in HSA/CAT@Ce6 catalyzes hydrogen peroxide in tumors to produce oxygen and then converts the oxygen into singlet oxygen through Ce6 under laser irradiation; this readily kills cancer cells. To characterize the catalytic activity, Ce6, CAT, and HSA/CAT@Ce6 were added, respectively, to PBS or H_2O_2 solution to observe the generation of oxygen bubbles (Figure S3). Optical photos show that no bubbles are generated in the experimental groups without hydrogen peroxide. In contrast, the HSA/CAT@Ce6 group and CAT group generate bubbles in the H_2O_2 solution, indicating catalytic activity. A commercial oxygen probe $[(Ru(dpp)_3)]Cl_2$ was used to detect the catalase-like capacity of HSA/CAT@Ce6. The results showed that the fluorescence intensity of the experimental group containing CAT was significantly lower than that of the experimental group without CAT, indicating that HSA/CAT@Ce6 has good catalase activity (Figure S6A). The singlet oxygen produced by HSA/CAT@Ce6 nanocapsules was detected using singlet oxygen sensor green (SOSG). As shown in Figure 2E, singlet oxygen gradually increases with laser irradiation time before finally reaching equilibrium, and the generation rate and total amount of the singlet oxygen group significantly increase after the addition of H_2O_2. In addition, singlet oxygen production increases with the concentration of hydrogen peroxide (Figure 2F).

In order to evaluate the biomedical applications of the flexible nanocapsules, the CCK8 method was used to test the cytotoxicity of flexible HSA/CAT and HSA/CAT@Ce6 in 4T1 tumor cells. The results show that the relative cellular activities have exceeded 80% after incubation with HSA/CAT and HSA/CAT@Ce6 for 24 h at concentrations of 0–200 μg/mL, and that the activity values have increased to 90% at material concentrations of 0–50 μg/mL. This indicates that the flexible protein nanocapsules have good biocompatibility (Figure 3A and B). The excellent biocompatibility of HSA/

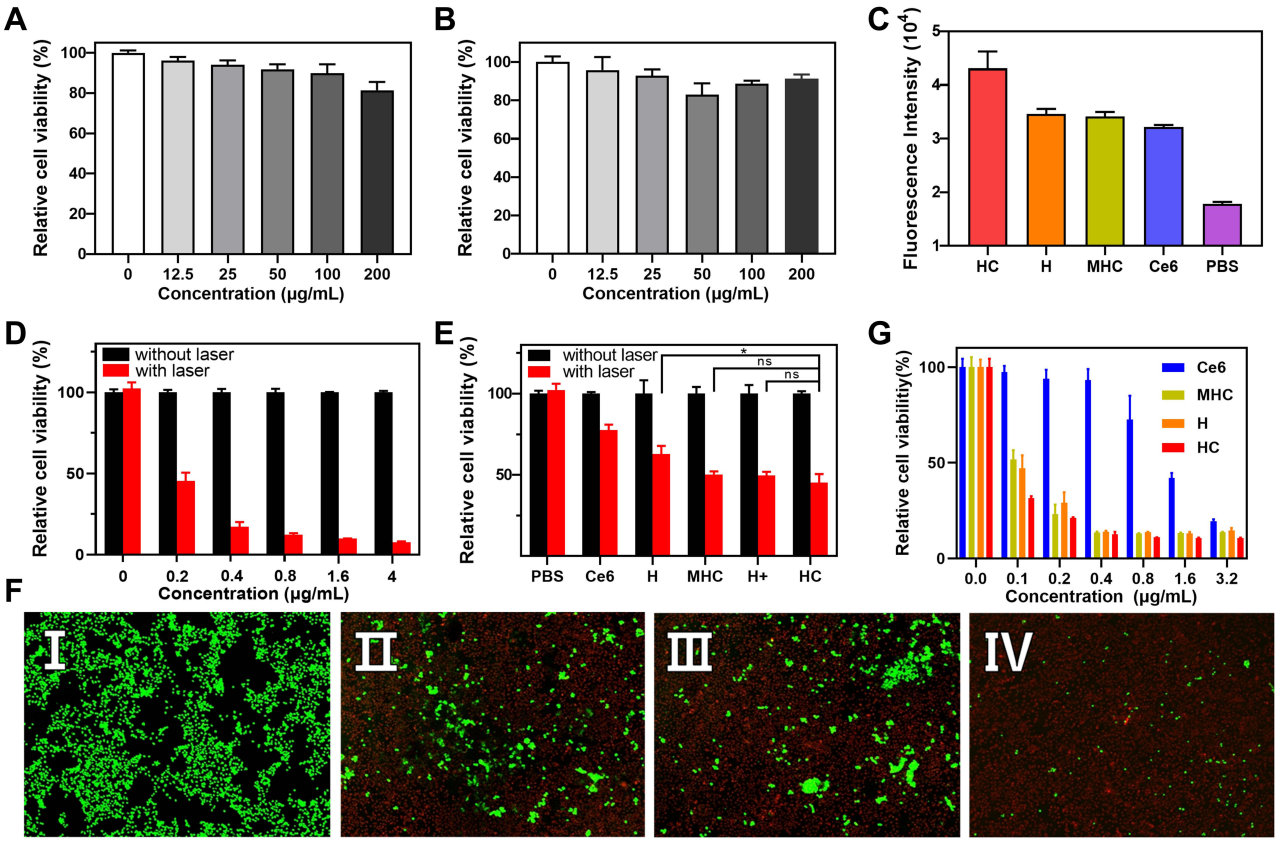

Figure 3 Relative cell viabilities of the 4T1 tumor cells with different concentrations of HSA/CAT (**A**) and HSA/CAT@Ce6 (**B**) after incubation for 24 h. (**C**) DCFH-DA fluorescence intensity of the 4T1 tumor cells incubated with PBS, free Ce6 (Ce6), HSA@Ce6 (H), MSNs-HSA/CAT@Ce6 (MHC), and HSA/CAT@Ce6 (HC), all with the same Ce6 concentration (3 μg/mL) and all exposed to laser irradiation (660 nm, 1 W/cm^2, 5 min). The 4T1 tumor cells incubated with PBS formed the control group (PBS). (**D**) Relative viabilities of 4T1 tumor cells incubated with different concentrations of HSA/CAT@Ce6 nanocapsules with or without laser irradiation. (**E**) Relative viabilities of 4T1 tumor cells incubated with free Ce6 (Ce6), HSA@Ce6 (H), MSNs-HSA/CAT@Ce6 (MHC), HSA+HSA/CAT@Ce6 (H+), and HSA/CAT@Ce6 (HC), all with the same Ce6 concentration (1.5 μg/mL), with or without laser irradiation. 4T1 tumor cells incubated with PBS formed the control group (PBS). *P* values: ns $P > 0.05$, $^*P < 0.05$ are calculated by SPSS with a *t*-test. (**F**) The live/dead staining of 4T1 tumor cells incubated with HSA/CAT@Ce6 (I), HSA@Ce6 + laser irradiation (II), MSNs-HSA/CAT@Ce6 + laser irradiation (III), and HSA/CAT@Ce6 + laser irradiation (IV). Scale bars: 200 μm. (**G**) Relative cell viabilities of the 4T1 tumor cells with different concentrations of Ce6, HSA@Ce6 (H), MSNs-HSA/CAT@Ce6 (MHC), and HSA/CAT@Ce6 (HC) with laser irradiation (5 min, 1 W/cm^2, 660 nm).

CAT and HSA/CAT@Ce6 lies in HSA and CAT being endogenous proteins, which are not very damaging to cells. Afterwards, the intracellular ROS contents generated by HSA/CAT@Ce6 were measured using DCFH-DA and compared with HSA@Ce6 (HSA/CAT@Ce6 without CAT), MSNs-HSA/CAT@Ce6 (HSA/CAT@Ce6 without etching silica spheres), and free Ce6 (Figure 3C). The results show that the fluorescence intensities of the experimental group containing Ce6 (HSA@Ce6, MSNs-HSA/CAT@Ce6, and HSA/CAT@Ce6) are all higher than those of the PBS group, indicating that Ce6 loaded at nanocapsules readily generates ROS under irradiation. The fluorescence intensity of the HSA@Ce6 group is higher than that of the free Ce6 group because the flexible protein nanoplatforms increase the cellular uptake of the photosensitizer. In addition, the fluorescence intensity of the HSA/CAT@Ce6 group is higher than that of the HSA@Ce6 group, demonstrating that the CAT contained in the HSA/CAT@Ce6 increases intracellular ROS production by catalyzing endogenous hydrogen peroxide in tumor cells. Furthermore, the fluorescence intensity of the HSA/CAT@Ce6 group is higher than that of the MSNs-HSA/CAT@Ce6 group. This suggests that the flexible hollow structure improves the cellular uptake, so as to effectively improve intracellular ROS production.

Subsequently, the in vitro PDT effects of HSA/CAT@Ce6 were studied using 4T1 cells. The results show that HSA/CAT@Ce6 readily kills 4T1 cells after laser irradiation (5 min, 1 W/cm^2, 660 nm), and that the killing efficacy increases with material concentration (Figure 3D). The PDT in vitro efficacy of the HSA/CAT@Ce6 was further compared with free Ce6 at a constant Ce6 concentration (1.5 μg/mL). The results show that the relative cell activity of free Ce6 with laser irradiation is more than 75%, while that of HSA/CAT@Ce6 (with the same concentration of Ce6) is less than 50% (Figure 3E). This means the cell killing efficiency of HSA/CAT@Ce6 is more than twice that of free Ce6. The origin of the relatively poor killing effect of Ce6 lies in it being a small molecule; it experiences difficulty in entering tumor cells and can leave cells freely, leading to a low cellular uptake efficiency. HSA/CAT@Ce6 is about 330 nm, which can be endocytosed by endoplasmic reticulum and retained in cells, increasing the concentration of Ce6 in cells. To illustrate the catalytic effect and flexible properties for enhancing PDT, HSA@Ce6 without adding CAT and MSNs-HSA/CAT@Ce6 without etching silica spheres were synthesized, and the in vitro PDT efficacies were compared with HSA/CAT@Ce6 (Figure 3E). The results show that the relative cell activity of the HSA/CAT@Ce6 group is significantly lower than that of the HSA@Ce6 group, indicating that CAT improves PDT efficacy by catalyzing endogenous hydrogen peroxide in tumor cells to generate oxygen for PDT. The relative cell activity of HSA/CAT@Ce6 is lower than that of solid MSNs-HSA/CAT@Ce6, indicating that the flexible properties are conducive to improving PDT efficacy by increasing the cellular uptake of Ce6. 4T1 tumor cells were incubated with HSA, and then HSA/CAT@Ce6 was added (HSA+HSA/CAT@Ce6) for PDT (Figure 3E). The relative cell activity of the HSA+HSA/CAT@Ce6 group is higher than that of the control group (HSA/CAT@Ce6) under the same conditions, indicating that HSA helps to improve PDT efficacy. This improvement is due to HSA's ability to bind to gp60 receptors on cells, thereby improving cell ingestion efficiency. The IC50 of HSA/CAT@Ce6, HSA@Ce6, MSNs-HSA/CAT@Ce6, and Ce6 are 0.044 μg/mL, 0.081 μg/mL, 0.092 μg/mL, and 1.232 μg/mL, respectively. The IC50 of HSA/CAT@Ce6 is smaller than that of the other three groups, which also proves that HSA/CAT@Ce6 has the strongest lethality to tumor cells. Furthermore, the in vitro PDT effects of HSA/CAT@Ce6 were studied using normal mammary epithelial cells (MCF 10A). As shown in Figure S4, under the same concentration and laser irradiation, the damage of HSA/CAT@Ce6 nanocapsules to normal cells was significantly less than that of tumor cells. Images of live and dead cell staining show that HSA/CAT@Ce6 nanocapsules kill almost all 4T1 cells under laser irradiation (Figure 3FI and FIV), while more living cells are found in the MSNs-HSA/CAT@Ce6 and HSA@Ce6 groups (Figure 3FII and FIII). This demonstrates that the flexible hollow structure and CAT significantly improve PDT efficacy.

Higher tumor accumulation and cellular uptake of nanoplatforms are generally related to better therapeutic outcomes.[29,30,32] Thus, the in vitro cellular uptake and targeting ability of HSA/CAT@Ce6 were evaluated using 4T1 cells. CLSM images show that the fluorescence intensity of flexible hollow HSA/CAT@Ce6 nanocapsules is stronger than that of rigid MSNs-HSA/CAT@Ce6 nanoparticles when 4T1 cells were incubated with them for 6 h (Figure 4A). In addition, we quantified relative Ce6 fluorescence intensity and the Ce6 mean fluorescence intensity. As shown in Figure S5A and S5B, the cellular internalization of HSA/CAT@Ce6 was significantly higher than that of MSNs-HSA/CAT@Ce6 and Ce6. These results demonstrate that the flexible hollow structure readily improves cellular uptake. To further evaluate the in vivo targeting ability of HSA/CAT@Ce6, mice with 4T1 tumors were intravenously injected with HSA/CAT@Ce6, MSNs-HSA/CAT@Ce6, or free Ce6, and the

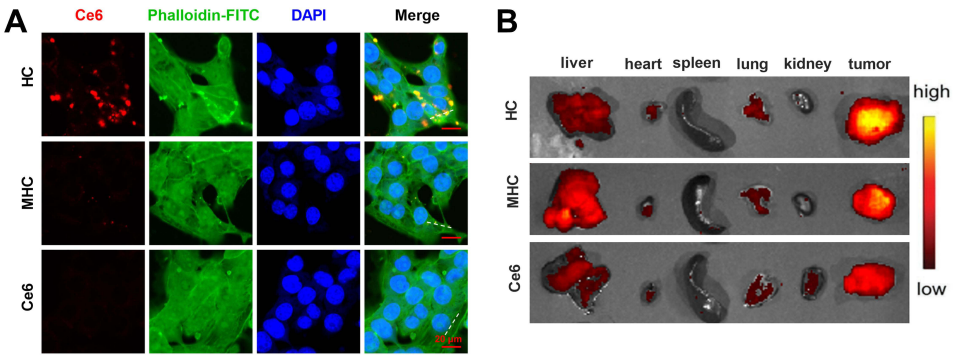

Figure 4 (**A**) CLSM images of 4T1 tumor cells after incubation with HSA/CAT@Ce6, MSNs-HSA/CAT@Ce6, and Ce6 for 6 h. Scale bars: 20 μm. Green, phalloidin-FITC; red, Ce6; blue, nucleus. (**B**) In vivo fluorescence images of harvested major organs and tumors from the mice with 4T1 tumor after the injection of free Ce6, HSA/CAT@Ce6, and MSNs-HSA/CAT@Ce6, all with the same Ce6 concentration.

fluorescence intensity of the major organs and tumor were examined using an in vivo imaging system. Live fluorescent images show that the flexible hollow HSA/CAT@Ce6 nanocapsules have the strongest fluorescence intensity, while the rigid solid MSNs-HSA/CAT@Ce6 nanoparticles have a medium intensity; the free Ce6 has the lowest fluorescence intensity (Figure 4B). This result is consistent with in vitro cell experiments which indicate that a protein capsule vector with a flexible hollow structure provides considerable in vivo tumor accumulation.

Because of the efficient uptake and targeting ability of HSA/CAT@Ce6, the PDT efficacy of flexible hollow protein capsules was studied in vivo. The mice received different treatments (HSA/CAT@Ce6 group, HSA@Ce6 group, MSNs-HSA/CAT@Ce6 group, and free Ce6 group; PBS group as a blank control group) 10 days after tumor inoculation. Changes in body weight and tumor volume over a period of 14 days were observed (Figure 5A). The weight of each group of mice is relatively stable, with no significant abnormal changes during the 14 days after treatment (Figure 5B). This indicates that all nanocapsules have no obvious systemic toxicity. Figure 5C shows the tumor volume changes in mice over the 14 days after receiving different injections with the same Ce6 concentration and laser irradiation. The volumes of the 4T1 tumor in the PBS treatment group continue to increase, indicating that laser irradiation alone does not inhibit tumor growth (Figure 5D). The volumes of the 4T1 tumor in the treatment group containing Ce6 decrease significantly after laser irradiation, indicating that PDT does kill tumor cells (Figures 5E–H). However, the tumor volumes in the HSA@Ce6 (Figure 5E), MSNs-HSA/CAT@Ce6 (Figure 5F), and free Ce6 (Figure 5G) treatment groups increase between the second and fourteenth days after treatment, reaching their maximum tumor volume on the 14th day. This indicates that these three treatment groups can only slightly inhibit the growth of tumor volume rather than completely ablate tumors. This result may be related to oxygen deficiency and poor PDT efficacy. MSNs-HSA/CAT@Ce6 nanocapsules have solid structures, and their tumor uptake, therefore, is relatively poor compared with that of flexible HSA/CAT@Ce6 nanocapsules. Free Ce6 lacks a drug delivery platform and targeting ability, generating the worst treatment effect. In contrast, the tumor volumes in the HSA/CAT@Ce6 treatment group do not increase markedly within 14 days after treatment (Figure 5H). The tumor volumes in the mice that receive HSA/CAT@Ce6 treatment also show the smallest size on the 14th day (Figure 5I). This suggests that HSA/CAT@Ce6 nanocapsules have the best PDT efficacy out of all the treatment groups. Therefore, the flexible properties and the two proteins of the HSA/CAT@Ce6 significantly enhance PDT efficacy. This is illustrated by the optical photos of tumors for different treatment groups on the 14th day (Figure S6B). Hematoxylin and eosin (H&E) staining images (Figure 5J) show that the necrotic areas in the HSA/CAT@Ce6 group are larger than those in the other groups (PBS, HSA@Ce6, MSNs-HSA/CAT@Ce6, and free Ce6 groups). This highlights the high PDT efficacy of flexible HSA/CAT@Ce6 nanocapsules. No obvious damage or inflammation is observed in the pathological sections of normal tissues (heart, liver, spleen, lungs, and kidneys), indicating that flexible HSA/CAT@Ce6 nanocapsules have good biocompatibility (Figure S7).

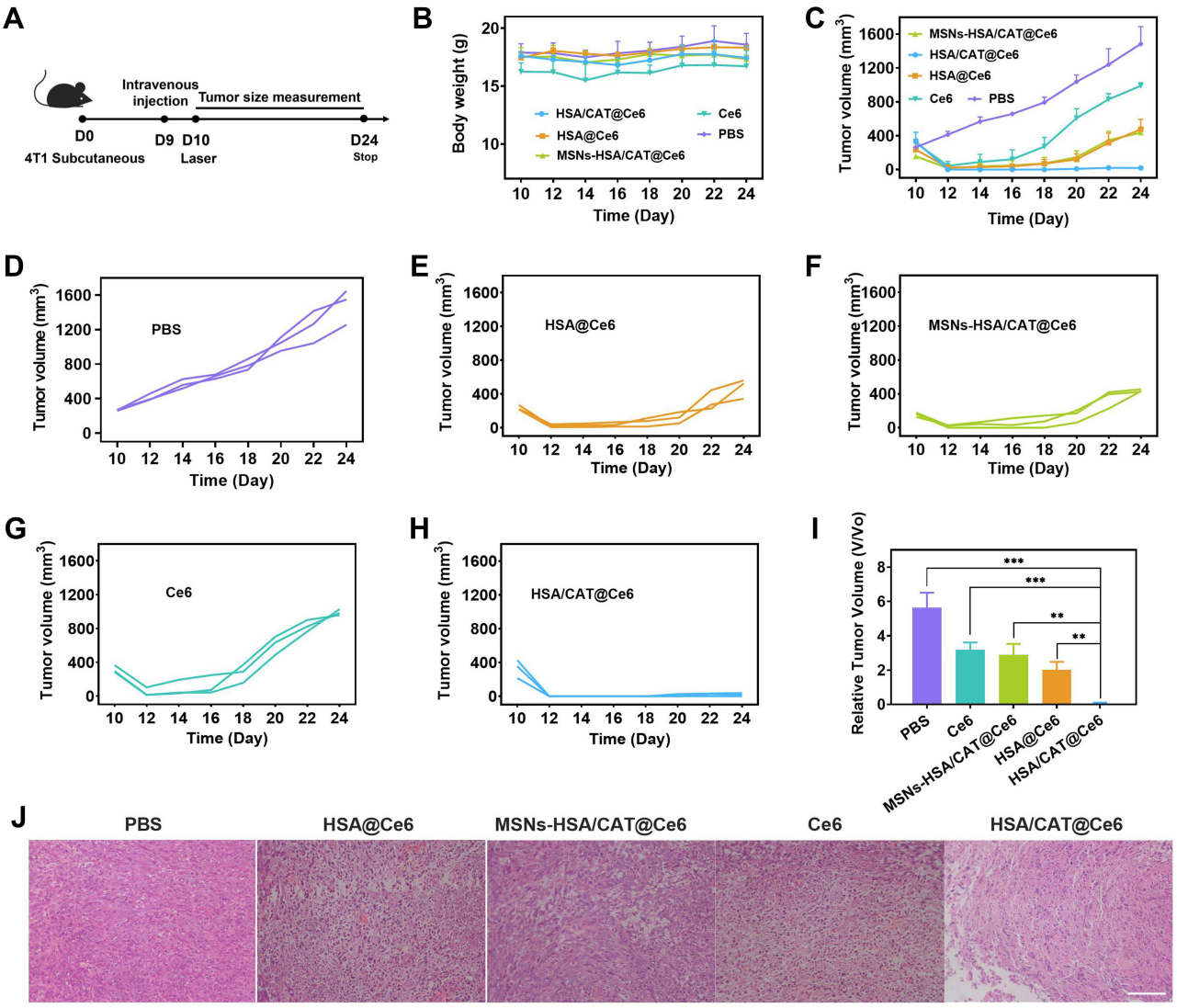

Figure 5 (**A**) Schematic diagram of the animal experiment. (**B**) Body weight change curve of the mice with 4T1 tumors in different groups (PBS, HSA@Ce6, MSNs-HSA/CAT@Ce6, free Ce6, and HSA/CAT@Ce6 groups) during the 14 days. (**C**) Tumor volume change curves of mice in different groups with the same Ce6 concentration and laser irradiation over 14 days. The tumor volume change curves of mice injected with (**D**) PBS, (**E**) HSA@Ce6, (**F**) MSNs-HSA/CAT@Ce6, (**G**) free Ce6, and (**H**) HSA/CAT@Ce6. (**I**) Relative tumor volumes on the 14th day in different groups. *P* values: $^{**}P < 0.01$, $^{***}P < 0.001$ are calculated by SPSS with a *t*-test. (**J**) H&E staining images of tissue sections from tumors with different treatments after 14 days. The parameters of the laser irradiation are 660 nm, 5 min, 1 W/cm^2. Scale bars:100 μm.

Conclusion

In summary, we successfully synthesized flexible hollow HSA/CAT nanocapsules using a core-assisted protein-coating approach. The HSA/CAT nanocapsules had a flexible character, uniform diameter (310 nm), and well-defined hollow structure. After loading photosensitizer, the HSA/CAT@Ce6 nanocapsules exhibited a higher cellular uptake and tumor targeting ability than their solid counterparts and free Ce6. Simultaneously, the HSA/CAT@Ce6 nanocapsules considerably increased the production of ROS through the catalytic ability of CAT to enhance PDT. The results of in vitro and in vivo experiments showed that the flexible hollow HSA/CAT@Ce6 nanocapsules greatly improved PDT efficacy without significant toxicity or side effects. Due to the excellent targeting and uptake ability of these flexible hollow protein nanocapsules, we believe they form part of an approach to improve PDT efficacy, and to potentially improve other treatments.

Acknowledgments

This work was supported by the National Natural Science Foundation of China (Nos. 81901806, 81971675, 21603106), the National Key Research and Development Program of China (Nos. 2017YFA0205301, 2017YFA0205302), the Key Research and Development Program of Jiangsu (No. BE2018732), the Natural Science Foundation of Jiangsu Province (No. BK20160017), and the State Key Laboratory of Analytical Chemistry for Life Science (No. 5431ZZXM1717).

Disclosure

The authors report no conflicts of interest in this work.

References

1. Chattopadhyay S, Liu Y-H, Fang Z-S, et al. Synthetic immunogenic cell death mediated by intracellular delivery of STING Agonist nanoshells enhances anticancer chemo-immunotherapy. *Nano Lett*. 2020;20(4):2246–2256. doi:10.1021/acs.nanolett.9b04094
2. Chen G, Yang Y, Xu Q, et al. Self-amplification of tumor oxidative stress with degradable metallic complexes for synergistic cascade tumor therapy. *Nano Lett*. 2020;20(11):8141–8150. doi:10.1021/acs.nanolett.0c03127
3. Liang X, Chen M, Bhattarai P, et al. Perfluorocarbon@Porphyrin nanoparticles for tumor hypoxia relief to enhance photodynamic therapy against liver metastasis of colon cancer. *ACS Nano*. 2020;14(10):13569–13583. doi:10.1021/acsnano.0c05617
4. Dolmans DE, Fukumura D, Jain RK. Photodynamic therapy for cancer. *Nat Rev Cancer*. 2003;3(5):380–387. doi:10.1038/nrc1071
5. Dougherty TJ. Photodynamic Therapy. *Photochem Photobiol*. 1993;58(6):895–900. doi:10.1111/j.1751-1097.1993.tb04990.x
6. Henderson BW, Dougherty TJ. How does photodynamic therapy work? *Photochem Photobiol*. 2010;55(1):145–157. doi:10.1111/j.1751-1097.1992.tb04222.x
7. Li H, Sun Z, Jiang S, et al. Tadpole-like unimolecular nanomotor with Sub-100 nm size swims in a tumor microenvironment model. *Nano Lett*. 2019;19(12):8749–8757. doi:10.1021/acs.nanolett.9b03456
8. Mokoena D, George BP, Abrahamse H. Conjugation of hypericin to gold nanoparticles for enhancement of photodynamic therapy in MCF-7 breast cancer cells. *Pharmaceutics*. 2022;14(10):2212. doi:10.3390/pharmaceutics14102212
9. Ibarra LE, Camorani S, Agnello L, et al. Selective photo-assisted eradication of triple-negative breast cancer cells through aptamer decoration of doped conjugated polymer nanoparticles. *Pharmaceutics*. 2022;14(3):626. doi:10.3390/pharmaceutics14030626
10. Lucky SS, Soo KC, Zhang Y. Nanoparticles in photodynamic therapy. *Chem Rev*. 2015;115(4):1990–2042. doi:10.1021/cr5004198
11. Mahdavi M, Fattahi A, Nouranian S. Doxorubicin stability and retention on PEGylated graphene oxide nanocarriers adjacent to human serum albumin. *ACS Appl Bio Mater*. 2020;3(11):7646–7653. doi:10.1021/acsabm.0c00843
12. Ruan Y, Jia X, Wang C, et al. Methylene blue loaded cu–tryptone complex nanoparticles: a new glutathione-reduced enhanced photodynamic therapy nanoplatform. *ACS Biomater Sci Eng*. 2019;5(2):1016–1022. doi:10.1021/acsbiomaterials.8b01398
13. Tian B, Wang C, Zhang S, et al. Photothermally enhanced photodynamic therapy delivered by nano-graphene oxide. *ACS Nano*. 2011;5(9):7000–7009. doi:10.1021/nn201560b
14. Wang D, Wu H, Yang G, et al. Metal–organic framework derived multicomponent nanoagent as a reactive oxygen species amplifier for enhanced photodynamic therapy. *ACS Nano*. 2020;14(10):13500–13511. doi:10.1021/acsnano.0c05499
15. Teng Z, Wang C, Tang Y, et al. Deformable hollow periodic mesoporous organosilica nanocapsules for significantly improved cellular uptake. *J Am Chem Soc*. 2018;140(4):1385–1393. doi:10.1021/jacs.7b10694
16. Yu M, Xu L, Tian F, et al. Rapid transport of deformation-tuned nanoparticles across biological hydrogels and cellular barriers. *Nat Commun*. 2018;9(1):2607–2614. doi:10.1038/s41467-018-05061-3
17. Fan L, Xu X, Zhu C, et al. Tumor catalytic–photothermal therapy with yolk–shell Gold@Carbon nanozymes. *ACS Appl Mater Interfaces*. 2018;10(5):4502–4511. doi:10.1021/acsami.7b17916
18. Hua X-W, Bao Y-W, Zeng J, et al. Ultrasmall all-in-one nanodots formed via carbon dot-mediated and albumin-based synthesis: multimodal imaging-guided and mild laser-enhanced cancer therapy. *ACS Appl Mater Interfaces*. 2018;10(49):42077–42087. doi:10.1021/acsami.8b16065
19. Wang P, Liang C, Zhu J, et al. Manganese-based nanoplatform as metal ion-enhanced ROS generator for combined chemodynamic/photodynamic therapy. *ACS Appl Mater Interfaces*. 2019;11(44):41140–41147. doi:10.1021/acsami.9b16617
20. Chen Q, Wang X, Wang C, et al. Drug-induced self-assembly of modified albumins as nano-theranostics for tumor-targeted combination therapy. *ACS Nano*. 2015;9(5):5223–5233. doi:10.1021/acsnano.5b00640
21. Peng X, Chen K, Liu W, et al. Soft mesoporous organosilica nanoplatforms improve blood circulation, tumor accumulation/penetration, and photodynamic efficacy. *Nano-Micro Lett*. 2020;12(1):137. doi:10.1007/s40820-020-00465-7
22. Xu C, Teng Z, Zhang Y, et al. Flexible MoS2-embedded human serum albumin hollow nanocapsules with long circulation times and high targeting ability for efficient tumor ablation. *Adv Funct Mater*. 2018;28(45):1804081. doi:10.1002/adfm.201804081
23. Park J, Jackman J, Ferhan A, et al. Cloaking silica nanoparticles with functional protein coatings for reduced complement activation and cellular uptake. *ACS Nano*. 2020;14(9):11950–11961. doi:10.1021/acsnano.0c05097
24. Zhang Q, Kuang G, He S, et al. Photoactivatable prodrug-backboned polymeric nanoparticles for efficient light-controlled gene delivery and synergistic treatment of platinum-resistant ovarian cancer. *Nano Lett*. 2020;20(5):3039–3049. doi:10.1021/acs.nanolett.9b04981
25. de la Rica R, Matsui H. Applications of peptide and protein-based materials in bionanotechnology. *Chem Soc Rev*. 2010;39(9):3499–3509. doi:10.1039/b917574c
26. Chen Z, He Y, Shi B, et al. Human serum albumin from recombinant DNA technology: challenges and strategies. *Biochim Biophys Acta*. 2013;1830(12):5515–5525. doi:10.1016/j.bbagen.2013.04.037
27. Zhu K, Lv T, Qin T, et al. A flavonoid-based fluorescent probe enables the accurate quantification of human serum albumin by minimizing the interference from blood lipids. *Chem Comm*. 2019;55(93):13983–13986. doi:10.1039/c9cc08015e

28. Zhu J, Xiao T, Zhang J, et al. Surface-charge-switchable nanoclusters for magnetic resonance imaging-guided and glutathione depletion-enhanced photodynamic therapy. *ACS Nano*. 2020;14(9):11225–11237. doi:10.1021/acsnano.0c03080
29. Wang S, Tian Y, Tian W, et al. Selectively sensitizing malignant cells to photothermal therapy using a CD44-targeting heat shock protein 72 depletion nanosystem. *ACS Nano*. 2016;10(9):8578–8590. doi:10.1021/acsnano.6b03874
30. Piao J-G, Wang L, Gao F, et al. Erythrocyte membrane is an alternative coating to polyethylene glycol for prolonging the circulation lifetime of gold nanocages for photothermal therapy. *ACS Nano*. 2014;8(10):10414–10425. doi:10.1021/nn503779d
31. Teng Z, Su X, Zheng Y, et al. A facile multi-interface transformation approach to monodisperse multiple-shelled periodic mesoporous organosilica hollow spheres. *J Am Chem Soc*. 2015;137(24):7935–7944. doi:10.1021/jacs.5b05369
32. Yuwen L, Zhou J, Zhang Y, et al. Aqueous phase preparation of ultrasmall MoSe2 nanodots for efficient photothermal therapy of cancer cells. *Nanoscale*. 2016;8(5):2720–2726. doi:10.1039/C5NR08166A
33. Liu Y, Ding L, Wang D, et al. Hollow Pd nanospheres conjugated with Ce6 to simultaneously realize photodynamic and photothermal therapy. *ACS Appl Bio Mater*. 2018;1(4):1102–1108. doi:10.1021/acsabm.8b00318
34. Dehvari K, Li J-D, Chang J-Y. Bovine serum albumin-templated synthesis of manganese-doped copper selenide nanoparticles for boosting targeted delivery and synergistic photothermal and photodynamic therapy. *ACS Appl Bio Mater*. 2019;2(7):3019–3029. doi:10.1021/acsabm.9b00339